JACS
JOURNAL OF THE AMERICAN CHEMICAL SOCIETY
Article
Cite This: J. Am. Chem. Soc. 2019, 141, 2342−2347
pubs.acs.org/JACS

Rapid Room-Temperature Synthesis of a Metastable Ordered Intermetallic Electrocatalyst

Yunfei Wang,[†] Du Sun,[†] Tomojit Chowdhury,[‡] Justine S. Wagner,[†] Thomas J. Kempa,[†,‡] and Anthony Shoji Hall*[,†]

[†]Department of Materials Science and Engineering, Johns Hopkins University, Baltimore, Maryland 21218, United States
[‡]Department of Chemistry, Johns Hopkins University, Baltimore, Maryland 21218, United States

Supporting Information

ABSTRACT: Metal alloys with atomic scale ordering (ordered intermetallics) have emerged as a new class of high performance materials for mediating electrochemical reactions. However, ordered intermetallic nanostructures often require long synthesis times and/or high temperature annealing to form because a high-activation energy barrier for interdiffusion must be overcome for the constituent metals to equilibrate into ordered structures. Here we report the direct synthesis of metastable ordered intermetallic $Pd_{31}Bi_{12}$ at room-temperature in minutes via electrochemical deposition. $Pd_{31}Bi_{12}$ is highly active for the reduction of O_2 to H_2O, delivering specific activities over 35× higher than those of commercial Pt and Pd nanocatalysts, placing it as the most active Pd-based catalyst, to the best of our knowledge, reported under similar testing conditions. Stability tests demonstrate minimal loss of activity after 10,000 cycles, and a retention of intermetallic crystallinity. This study demonstrates a new method of preparing ordered intermetallics with extraordinary catalytic activity at room temperature, providing a new direction in catalyst discovery and synthesis.

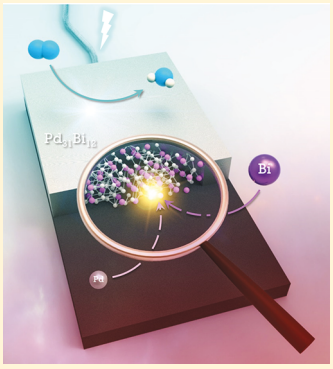

INTRODUCTION

Nanostructured precious metals are efficient catalysts for various renewable energy conversion and storage technologies.[1,2] The most common strategy for designing high performance electrocatalysts is to alloy precious metals with d-block transition metals, allowing the adsorption energy of reaction intermediates to be tuned toward more optimal values.[3] Recent results have demonstrated that some ordered intermetallic compounds (OICs) can outperform solid solution alloys of the same composition for the oxygen reduction reaction,[4−7] formic acid oxidation,[8] methanol oxidation,[9] and CO_2 reduction.[10] An OIC can exhibit drastically different electronic structure compared to its constituent elements, particularly when the crystal structure of the intermetallic differs from that of its parent elements.[11,12] However, most OICs composed of precious metals (e.g., Pt, Pd, Au, Cu, etc.) that are evaluated as electrocatalysts adopt the face-centered tetragonal crystal lattice (FCT), which can be thought of as a face-centered cubic lattice (FCC) that is slightly elongated along one axis. OICs having drastically reduced symmetry relative to their parent elements are rarely encountered in electrocatalysis.

The synthesis of nanoscale OICs is challenging because temperatures in excess of 700 °C are often required to facilitate interdiffusion and equilibration of atoms into atomically ordered structures.[6,13] Recently, methods utilizing high temperature annealing in silica shells and KCl matrixes have been developed to prepare nanoscale OICs.[14−16] OICs can be accessed by colloidal synthesis; however, this method is only viable for a narrow range of particle sizes and compositions due to competition with the formation of kinetically facile solid-solution phases.[5,9,17] The lack of accessible methods for synthesizing nanostructured OICs in mild conditions has stymied progress in the discovery of new catalysts. Synthetic methods allowing for the preparation of new OICs under mild reaction conditions have the potential accelerate catalyst development.

Electrodeposition is a flexible method that has been used to prepare OICs composed of non-noble metal elements for lithium-ion batteries,[18] lithium−sulfur batteries,[19] and thermoelectric devices.[20] However, this method is rarely used to prepare OICs for catalytic applications, due to the difficulty of precisely controlling the final material composition when codepositing precious metals and nonprecious metals.[21] Electrodeposition has several significant advantages over other synthetic methods for catalyst preparation, including the ability to grow directly on conductive substrates without postannealing or binding,[5,9] and the ability to modulate composition, crystallinity, and faceting.[22−26] Lastly, electrodeposition can fulfill the industrial demands of large-scale production.

Here, we report the direct preparation of $Pd_{31}Bi_{12}$ ordered intermetallic thin films at room temperature via electrochemical deposition from an aqueous electrolyte. Electrodeposition yields an OIC in minutes, while conventional nanoparticle synthesis or high temperature annealing methods require many hours for the synthesis to complete.[27−30] To the

Received: September 13, 2018
Published: January 16, 2019

DOI: 10.1021/jacs.8b09919
J. Am. Chem. Soc. 2019, 141, 2342−2347

best of our knowledge, electrodeposited $Pd_{31}Bi_{12}$ exhibits the highest specific activity measured among Pd-based materials for the oxygen reduction reaction (ORR). We demonstrate that the enhanced activity of $Pd_{31}Bi_{12}$ arises from a more favorable electron transfer coefficient and downshifted valence band center, relative to Pd.

RESULTS AND DISCUSSION

Room Temperature Synthesis of $Pd_{31}Bi_{12}$. $Pd_{31}Bi_{12}$ was deposited from a solution containing $Bi(C_2H_3O_2)_3$, Na_2PdCl_4, $C_{10}H_{16}N_2O_8$ (EDTA), and CH_3COOH. Cyclic voltammetry (CV) was used to assess the reduction potential of the Pd^{2+} and Bi^{3+} complexed with EDTA (Figure 1a) on glassy carbon

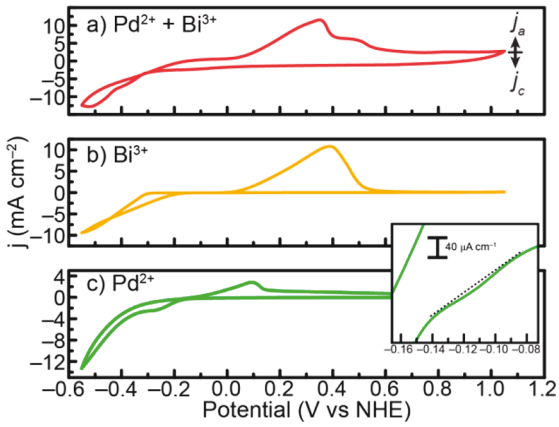

Figure 1. Cyclic voltammograms (CV) of solutions containing (a) 50 mM EDTA + 25 mM $Bi(C_2H_3O_2)_3$ + 4 mM Na_2PdCl_4, (b) 50 mM EDTA + 25 mM $Bi(C_2H_3O_2)_3$, and (c) 50 mM EDTA + 4 mM Na_2PdCl_4. All solutions were adjusted to pH 3.7 with acetic acid.All data was collected at 20 mV/s scan rate and is presented vs the normal hydrogen electrode (NHE). Inset: Zoom in of the −0.16 to 0.08 V vs NHE region for Pd^{2+} solution showing a small cathodic wave.

(GC) electrodes. To understand the origin of the redox features of this plating bath, we evaluated the electrochemical response of Bi^{3+} (Figure 1b) or Pd^{2+} (Figure 1c) salts with EDTA. The CV of Bi-EDTA exhibits a reductive wave which onsets at −0.20 V and can be attributed to the deposition of bulk Bi. As the scan direction is reversed, we observe a crossing point of the wave near −0.45 V and as the voltage is scanned more positively we observe an increased current density relative to the forward trace until −0.15 V. This so-called "crossing over" of the forward and reverse scans is indicative of a nucleation overpotential, where additional voltage is required to drive the deposition of the metal beyond its equilibrium potential. We observe a broad feature centered at 0.40 V in the reverse trace from the oxidative dissolution of Bi. For Pd-EDTA solution, we observe two cathodic waves at −0.11 and −0.25 V, and as the solution is scanned toward more negative voltages a sharp reductive wave is observed (Figure 1c). The small reductive wave at −0.11 V arises from a small amount of $[PdCl_3(H_2O)]^-$ ions which are present at concentrations of ∼1 μM assuming an equilibrium constant of 10^5 for Pd-EDTA-Cl complexes (Figure 1, inset).[31,32] The feature at −0.25 V arises from the deposition of Pd-EDTA-Cl complex, and the sharp reductive feature at more negative voltages arises predominately from H_2 evolution. In the mixed Pd−Bi bath, we observe the onset of a small wave which is attributable to the codeposition of Pd and Bi at −0.10 V and has an onset similar to the one observed for the deposition bath containing only Pd albeit with a larger current density. At this potential $[PdCl_3(H_2O)]^-$ ions deposit onto the electrode surface, and Bi^{3+} deposits onto the Pd nuclei via underpotential deposition (UPD). The other reductive features appear at more negative potentials. The oxidation of Bi in the mixed bath shifts to more negative potentials, while for Pd it shifts to more positive potentials, indicating that Bi is easier to oxidize, and Pd is more difficult to oxidize when deposited together. To prepare Pd−Bi intermetallic we applied a potential of −0.10 V for 1000 s and recorded a current density of ∼0.10 mA cm^{-2} (Figure S1). Before electrochemical evaluation, all the samples underwent a thorough cleaning process to remove organic residue from the surface of the films. Further details can be found in the Supporting Information (SI).

Characterization of Electrodeposited $Pd_{31}Bi_{12}$. X-ray diffraction (XRD) was used to identify the crystal structure of the deposited material (Figure 2a). Remarkably, the room

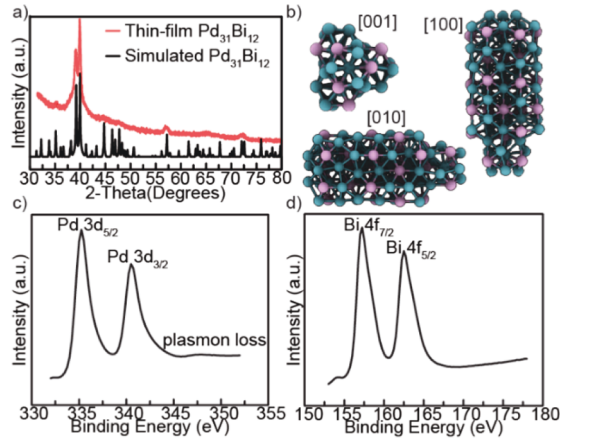

Figure 2. (a) XRD of electrodeposited $Pd_{31}Bi_{12}$ thin films. (b) Unit cell of $Pd_{31}Bi_{12}$ along three low index viewing directions. High resolution XPS spectra of the (c) Pd 3d region and (d) Bi 4f region of a $Pd_{31}Bi_{12}$ thin film.

temperature deposition yielded a phase pure, ordered intermetallic $Pd_{31}Bi_{12}$ (R3 space group).[33] The primary peaks match well with the diffraction pattern of $Pd_{31}Bi_{12}$, which can be differentiated from other Pd-rich phases, such as Pd_3Bi (Figure S2).[34,35] Differences in electronegativity and crystal structure between Pd (FCC) and Bi (rhombohedral) inhibit the formation of solid-solutions as indicated by the Pd−Bi phase diagram; allowing ordered phases to be accessed directly.[36] The phase diagram of Pd−Bi indicates that $Pd_{31}Bi_{12}$ is thermodynamically stable from 550 to 605 °C. Electrodeposition normally takes place under conditions far from equilibrium, especially when deposition is performed at large overpotentials, and therefore phases which are not accessible by conventional metallurgical processes can be accessed.[36,37] The two main reflections of $Pd_{31}Bi_{12}$ are broad relative to those in the simulated pattern suggesting that the sample contains a distribution of nanoscale grains with ∼35 nm diameter (Figure S3). $Pd_{31}Bi_{12}$ adopts a low symmetry crystal structure with a rhombohedral lattice (Figure 2b). X-ray photoelectron spectroscopy (XPS) was used to measure the oxidation state and composition of $Pd_{31}Bi_{12}$. The ratio of Pd to Bi according to an XPS survey scan is 73% Pd and 27% Bi,

DOI: 10.1021/jacs.8b09919
J. Am. Chem. Soc. 2019, 141, 2342−2347

which is within a percent of the theoretical value of $Pd_{31}Bi_{12}$ (72% Pd, 28% Bi). Hi-resolution XPS scans of $Pd_{31}Bi_{12}$ reveal the binding energy of the $3d_{5/2}$ and $3d_{3/2}$ levels to be 335.25 and 340.50 eV, respectively, indicating the oxidation state is similar to metallic Pd (Figure 2c). Evaluation of the Bi core levels reveals the Bi $4f_{7/2}$ and Bi $4f_{5/2}$ levels to be 157.25 and 162.50 eV respectively, indicating that the oxidation state is similar to elemental Bi (Figure 2d). Taken together, these data indicate the formation of a metallic $Pd_{31}Bi_{12}$ compound.

Scanning electron microscopy (SEM) images and atomic force microscopy (AFM) topographical maps of electrodeposited $Pd_{31}Bi_{12}$ identify a compact film consisting of a few layers of nanoparticles with diameters ranging between ~30 and 300 nm (Figures 3a,b and S4). High-resolution

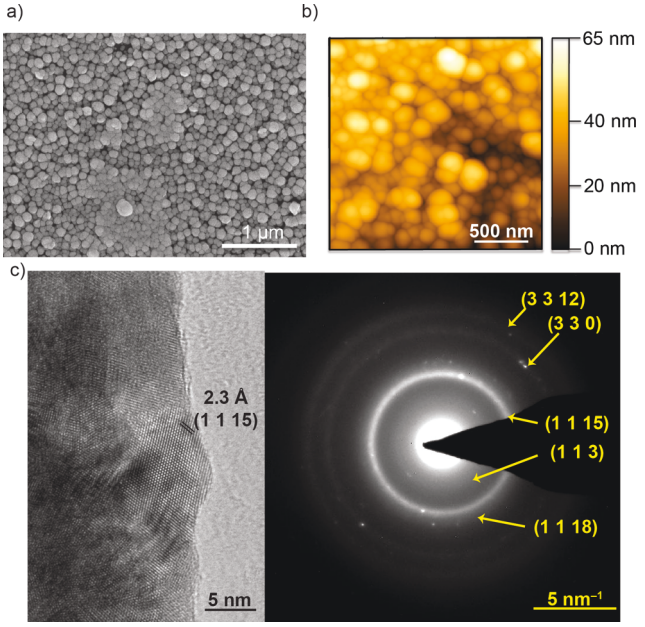

Figure 3. Representative (a) SEM image, (b) AFM map of the electrodeposited film, and (c) transmission electron microscopy (TEM) image of the electrodeposited film and the corresponding selected area electron diffraction (SAED) pattern which matches $Pd_{31}Bi_{12}$.

transmission electron microscopy (HRTEM) images indicate that the electrodeposited material is polycrystalline, with an observed lattice spacing of 2.3 Å that can be indexed to the (1 1 15) plane of $Pd_{31}Bi_{12}$ (Figure 3c). The observed rings and intensities in the Selected Area Electron Diffraction (SAED) pattern collected near the region near Figure 3c can be indexed to the (1 1 3), (1 1 15), (3 3 0), and (3 3 12) reflections of $Pd_{31}Bi_{12}$.

ORR Activity and Selectivity of $Pd_{31}Bi_{12}$. The activity of $Pd_{31}Bi_{12}$ for ORR was assessed on a 5 mm diameter GC rotating-disk electrode in O_2-saturated 0.1 M KOH electrolyte with a graphite rod counter electrode. We collected linear sweep voltammograms (LSV) on $Pd_{31}Bi_{12}$, Pt/C (TEC10E40E, TKK), and Pd/C (40% Pd on Vulcan XC-72, Premetek) at 1600 rpm to assess the ORR activity (Figures 4a and S5–S7). The electrochemical surface area (ECSA) was measured by CO stripping in 0.1 M KOH (Figures S8–S10). All ORR data are referenced to the reversible hydrogen electrode (RHE).

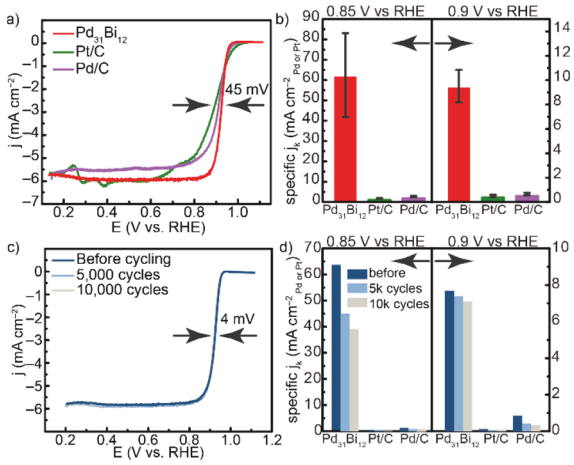

Figure 4. (a) Linear sweep voltammograms (LSV) collected at 1600 rpm. (b) Mass transport corrected specific activity at 0.85 and 0.90 V vs RHE. (c) LSVs and (d) Mass transfer corrected specific activity after 5000 and 10,000 cycles of accelerated durability testing collected at 1600 rpm.

The onset potential for ORR in $Pd_{31}Bi_{12}$ (0.96 V) is lower than Pt/C (0.99 V) and Pd/C (0.98 V). $Pd_{31}Bi_{12}$ exhibits a very steep slope near its onset potential for ORR, thereby allowing it to reach larger current densities at voltages < 0.95 V. The half-wave potential of $Pd_{31}Bi_{12}$ is 0.93 V, which is 28 mV higher than Pd/C and 45 mV higher than Pt/C, indicating that $Pd_{31}Bi_{12}$ exhibits superior activity compared to commercial Pt-group catalysts. To discern if ORR occurs via the two-electron ($2e^-$) or a four-electron ($4e^-$) pathway on $Pd_{31}Bi_{12}$, a Koutecky–Levich (KL) plot was constructed by measuring the steady-state chronoamperometry at various rotation rates.[38] KL analysis indicates the $4e^-$ reaction pathway is dominant throughout the entire potential range (Figure S11).

To directly compare the intrinsic activity of all of the catalysts, the Pd/Pt-based specific activities were averaged across three or more freshly prepared samples (Figure 4b). At 0.90 V, the specific activity of $Pd_{31}Bi_{12}$ (9.20 ± 1.41 mA/cm^2_{Pd}) is significantly higher than that of Pt/C (0.32 ± 0.12 mA/cm^2_{Pt}) and Pd/C (0.77 ± 0.17 mA/cm^2_{Pd}); and at 0.85 V, the specific activity of $Pd_{31}Bi_{12}$ (61.7 ± 20.73 mA/cm^2_{Pd}) is significantly higher than that of Pt/C (1.12 ± 0.15 mA/cm^2_{Pt}) and Pd/C (1.71 ± 0.21 mA/cm^2_{Pd}). The 10-fold to 35-fold enhancement of the specific activity of $Pd_{31}Bi_{12}$ occurs because it nearly reaches nearly diffusion limited current densities at 0.90 and 0.85 V, while Pt/C and Pd/C are far from reaching diffusion limited currents in the same range.

The specific activity of $Pd_{31}Bi_{12}$ was also compared to electrodeposited Pd- and Pt-thin films, which were prepared in the same way as $Pd_{31}Bi_{12}$ except the bath contained only Na_2PdCl_4 or Na_2PtCl_4 salts for the metal source. The resulting films exhibit similar surface area and morphology to electrodeposited $Pd_{31}Bi_{12}$ (Figures S11–S13). The specific activity of $Pd_{31}Bi_{12}$ is >10x or 15x higher than electrodeposited Pd- and Pt-thin films at 0.90 and 0.85 V, respectively (Figure S14), indicating that the specific activity of $Pd_{31}Bi_{12}$ is superior to both Pt/Pd nanoparticles and thin films.

The mass activity of the $Pd_{31}Bi_{12}$ thin film is comparable to Pt/C and Pd/C since increases in activity are negated by the large mass loading and reduced surface area to volume ratio of the electrodeposited films (Figures S15 and S16). These results indicate the preparation of highly dispersed $Pd_{31}Bi_{12}$

DOI: 10.1021/jacs.8b09919
J. Am. Chem. Soc. 2019, 141, 2342–2347

nanoparticles with small diameters have the possibility of exhibiting significantly improved mass activity compared to Pd/C and Pt/C.

Long-term stability was assessed via accelerated durability testing (ADT), which consists of repeatedly cycling the electrodes between 0.60 and 1.00 V at 100 mV/s in O_2-saturated electrolyte. The half-wave potential of $Pd_{31}Bi_{12}$ shifts by −4 mV after 10,000 cycles (Figure 4c); the negligible loss of half-wave potential indicates that $Pd_{31}Bi_{12}$ possesses extraordinary stability. The specific activity after 5000 and 10,000 cycles was measured to assess the catalyst stability (Figure 4d). At 0.90 V, the specific activity of $Pd_{31}Bi_{12}$ decreases from 7.6 to 7.1 mA/cm^2_{Pd} and at 0.85 V it decreases from 63 to 39 mA/cm^2_{Pd} after 10,000 cycles. The specific activity for Pd/C decreases from 0.77 to 0.31 mA/cm^2_{Pd} (0.9 V) and 1.80 to 0.91 mA/cm^2_{Pd} (0.85 V) and for Pt/C it decreases from 0.136 to 0.067 mA/cm^2_{Pt} (0.90 V) and from 0.51 to 0.26 mA/cm^2_{Pt} (0.85 V) after 10,000 cycles (Figures 4d, S18, and S19). The decrease in activity after ADT for $Pd_{31}Bi_{12}$ and Pt/C can be attributed to removal of highly active sites, given that the ECSA of these electrodes decreased by ∼10% after 10,000 cycles (Figure S20). In contrast, Pd/C exhibits a large decrease in activity for the first 5000 cycles, presumably caused by particle detachment as suggested by a ∼40% decrease in ECSA. Despite a decrease in specific activity after ADT for $Pd_{31}Bi_{12}$, it still maintains a ∼10 fold or more enhancement in specific activity relative to fresh Pt/C and Pd/C. After ADT, the ratio of Pd to Bi is ∼71% Pd to 29% Bi which is within a few percent of the fresh sample and theoretical composition (Figure S21). HRTEM images and SAED patterns on $Pd_{31}Bi_{12}$ after the 10,000 cycles indicates that the intermetallic crystallinity of $Pd_{31}Bi_{12}$ is retained (Figure S22).

Mechanistic Insights of $Pd_{31}Bi_{12}$ during ORR. To provide insight into the mechanism of ORR on $Pd_{31}Bi_{12}$, we performed electrokinetic measurements. Tafel slopes $\left(\frac{dE}{d\log(j)}\right)$ were measured by steady-state chronoamperometry, corrected for mass transport effects by the K-L method, and normalized by the ECSA (Figure 5). $Pd_{31}Bi_{12}$ exhibits two Tafel slopes depending on the applied overpotential (η); for η < 0.30 V a 21 mV/dec Tafel slope is observed, while for η > 0.30 V a 58 mV/dec Tafel slope is observed. A Tafel slope of 24 and 58 mV/dec corresponds to a transfer coefficient, $\alpha = \frac{2.303RT}{F}\left(\frac{dE}{d\log(j)}\right)^{-1}$, of 1.0 and 2.9, respectively. For Pd, the Tafel slope is 54 mV/dec at low overpotentials and 193 mV/dec at larger overpotentials, corresponding to an α of 1.0 and 0.31, respectively. The transfer coefficient (α) provides information about the number of electrons transferred between the resting state and the rate-limiting step of the catalytic cycle, and the fraction of the interfacial potential that lowers the free energy barrier of the reaction.[39,40] Therefore, a larger α (smaller Tafel slope) is desirable from a kinetic perspective as a smaller change in the applied voltage will lead to a larger increase in the reaction rate.

The exchange current density, i_0, of $Pd_{31}Bi_{12}$ is 3 orders of magnitude lower than Pd in both Tafel regions, indicating that it exhibits lower intrinsic activity at equilibrium (Figure 5B). However, $Pd_{31}Bi_{12}$ exhibits a larger α for both Tafel regions, indicating that $Pd_{31}Bi_{12}$ exhibits a lower barrier to electron transfer relative to Pd. The aggregate rate constant of a cathode, i_c, is dependent on both the exchange current density, i_0, and the transfer coefficient, α, as shown in eq 1, where R is

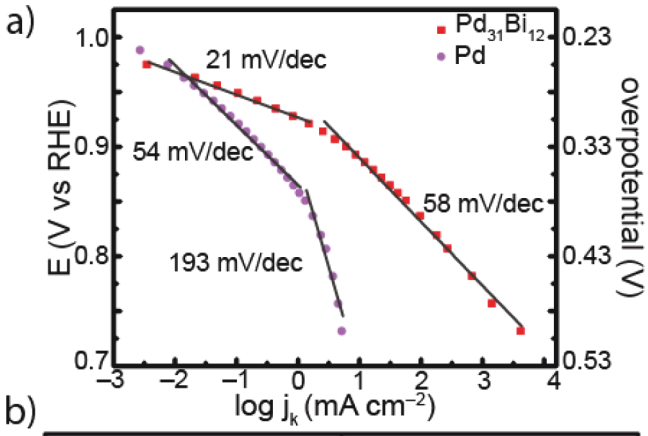

b)

$Pd_{31}Bi_{12}$				Pd			
Potential Range (V)	Tafel Slope (mv dec^{-1})	Transfer Coefficient (α)	I_0 (mA cm^{-2})	Potential Range (V)	Tafel Slope (mv dec^{-1})	Transfer Coefficient (α)	I_0 (mA cm^{-2})
0.97 ~ 0.92	21	2.9	7.5×10^{-7}	0.97 ~ 0.86	54	1.0	1.5×10^{-4}
0.91 ~ 0.73	58	1.0	9×10^{-5}	0.85 ~ 0.73	193	0.31	0.18

Figure 5. (a) Mass-transport corrected plot of voltage vs log current and (b) table of transfer coefficients, Tafel slopes, and exchange current density of $Pd_{31}Bi_{12}$ and Pd/C collected by steady state chronoamperometry in O_2-saturated 0.1 M KOH.

the universal gas constant, F is Faraday's constant, and T is temperature (in K). Indeed, as the voltage is increased, a larger fraction of the interfacial potential is used to lower the free energy barrier of the electrochemical reaction, allowing $Pd_{31}Bi_{12}$ to exhibit greater activity for η > 0.28 V (E < 0.95 V).

$$i_c = i_0\, e^{\alpha EF/RT} \quad (1)$$

The rate-limiting step of Pd and Pt surfaces is the 1e$^-$ reduction of O_2; this is consistent with a Tafel slope of 60 mV/dec at low overpotential and 120 mV/dec at higher overpotentials.[41,42] Although the Tafel slopes are different in both potential ranges, it is consistent with the same mechanism for a material with a decreasing population of kinetically incompetent coadsorbates, such as OH^-, as the overpotential is increased.[41,42] For $Pd_{31}Bi_{12}$, a Tafel slope of 60 mV/dec can indicate rate-limiting 1e$^-$ reduction of O_2 or chemical decomposition of surface adsorbed OOH, depending on the surface coverage of OH^- on the electrode surface; while a Tafel slope near 24 mV/dec indicates that the 1 e$^-$ reduction of surface adsorbed O is rate-limiting. However, it is difficult to propose a rate-limiting step from Tafel slopes alone due to its dependence on OH^- surface coverage. Hence, we will defer a mechanistic proposal to a more comprehensive study. Nevertheless, large differences in α between $Pd_{31}Bi_{12}$ and Pd indicate that the mechanism of ORR on $Pd_{31}Bi_{12}$ is different from that on Pd, contrary to what is observed with reported Pd and Pt alloys (Table S1).

Alloying Pd with Bi can serve to modify the electronic structure of Pd via (1) electronic effects which are sensitive to the composition and symmetry of the crystal, (2) the geometric effect which is related to the local arrangement of the active sites on the surface, and (3) ensemble effects which are related to the distribution of neighboring atoms on the surface of the catalyst for each atom.[3] Generally, such effects can give rise to lower adsorption energies of O_2-reaction

DOI: 10.1021/jacs.8b09919
J. Am. Chem. Soc. 2019, 141, 2342−2347

intermediates on Pt or Pd alloys, while leaving the reaction mechanism similar to the parent metal, as indicated by similar Tafel slopes (Table S1).

The electronic structure of a material dictates its catalytic activity since the adsorption energy of reaction intermediates is sensitive to the *d*-band center (valence band) of the material. A lower lying valence band center (relative to the Fermi level) is associated with weaker adsorbate binding due to a larger occupancy of the adsorbate's antibonding orbitals. Accordingly, a higher lying valence band relative to the Fermi level indicates stronger adsorbate binding.

To obtain insight regarding the modification of Pd by Bi alloying, we measured the valence band spectra of $Pd_{31}Bi_{12}$ and Pd foil with Ultraviolet Photoelectron Spectroscopy (UPS) with a He ion source (Figures 6, S23, and S24). The valence-

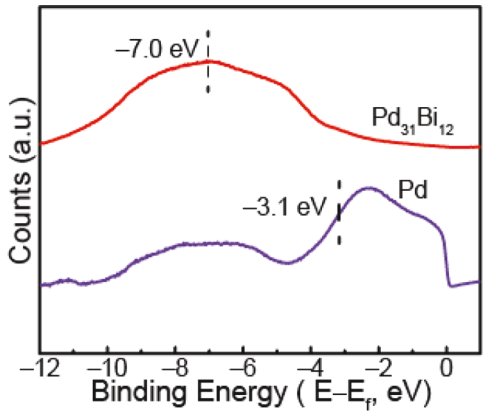

Figure 6. Valence band spectra of $Pd_{31}Bi_{12}$ and Pd foil collected by ultraviolet photoelectron spectroscopy (UPS) with a He I source.

band center of Pd lies at −3.1 eV, while the valence band center lies at −7 eV for $Pd_{31}Bi_{12}$. The lower lying valence band center of $Pd_{31}Bi_{12}$ implies that the adsorption energy of ORR intermediates is reduced relative to Pd. According to the Sabatier principle, Pd adsorbs oxygen-based intermediates too strongly, and hence, a reduction in adsorption energy should enhance catalysis.[43] Indeed, $Pd_{31}Bi_{12}$ exhibits superior catalytic reactivity relative to elemental Pd, indicating that alloying Pd with Bi shifts the adsorption energy of intermediates to more optimal values.

CONCLUSION

In conclusion, we have demonstrated that electrodeposition can be used to prepare thin films of ordered intermetallic $Pd_{31}Bi_{12}$ at room temperature. $Pd_{31}Bi_{12}$ is a highly active and stable material for mediating the reduction of O_2 to H_2O. The increased activity and stability of our material relative to other Pt-group metals is attributed to the formation of a Pd−Bi alloy with atomic scale ordering, reaching specific activities that exceed Pd and Pt by as much as 35-fold at 0.85 V, and 10-fold at 0.90 V. Interestingly, electrokinetic studies have indicated that the mechanism of O_2 reduction on $Pd_{31}Bi_{12}$ is different than that on elemental Pd. We ascribe this difference in mechanism to the formation of an OIC with significantly reduced symmetry relative to the highly symmetric elemental Pd. OICs containing Pd and metalloids are poised to serve as a promising new class of high performance electrocatalysts.

ASSOCIATED CONTENT

Supporting Information

The Supporting Information is available free of charge on the ACS Publications website at DOI: 10.1021/jacs.8b09919.

Full experimental details of nanoparticle film and thin film preparation, and characterization of the materials used in this article (PDF)

AUTHOR INFORMATION

Corresponding Author

*shoji@jhu.edu

ORCID

Thomas J. Kempa: 0000-0002-1672-8325

Anthony Shoji Hall: 0000-0003-4134-4160

Notes

The authors declare no competing financial interest.

ACKNOWLEDGMENTS

A.S.H. acknowledges financial support from the National Science Foundation under Award No. CHE-1764310 and Johns Hopkins University start-up funding.

REFERENCES

(1) Seh, Z. W.; Kibsgaard, J.; Dickens, C. F.; Chorkendorff, I.; Nørskov, J. K.; Jaramillo, T. F. Combining Theory and Experiment in Electrocatalysis: Insights into Materials Design. *Science* **2017**, *355* (6321), eaad4998.

(2) Möhle, S.; Zirbes, M.; Rodrigo, E.; Gieshoff, T.; Wiebe, A.; Waldvogel, S. R. Modern Electrochemical Aspects for the Synthesis of Value-Added Organic Products. *Angew. Chem., Int. Ed.* **2018**, *57*, 6018−6041.

(3) Liu, P.; Norskov, J. K. Ligand and Ensemble Effects in Adsorption on Alloy Surfaces. *Phys. Chem. Chem. Phys.* **2001**, *3*, 3814−3818.

(4) Cui, Z.; Chen, H.; Zhou, W.; Zhao, M.; DiSalvo, F. J. Structurally Ordered Pt_3Cr as Oxygen Reduction Electrocatalyst: Ordering Control and Origin of Enhanced Stability. *Chem. Mater.* **2015**, *27*, 7538−7545.

(5) Bu, L.; Shao, Q.; E, B.; Guo, J.; Yao, J.; Huang, X. PtPb/PtNi Intermetallic Core/Atomic Layer Shell Octahedra for Efficient Oxygen Reduction Electrocatalysis. *J. Am. Chem. Soc.* **2017**, *139* (28), 9576−9582.

(6) Meku, E.; Du, C.; Sun, Y.; Du, L.; Wang, Y.; Yin, G. Electrocatalytic Activity and Stability of Ordered Intermetallic Palladium-Iron Nanoparticles toward Oxygen Reduction Reaction. *J. Electrochem. Soc.* **2016**, *163*, F132−F138.

(7) Li, C.; Tan, H.; Lin, J.; Luo, X.; Wang, S.; You, J.; Kang, Y.-M.; Bando, Y.; Yamauchi, Y.; Kim, J. Emerging Pt-based Electrocatalysts with Highly Open Nanoarchitectures for Boosting Oxygen Reduction Reaction. *Nano Today* **2018**, *21*, 91−105.

(8) Gunji, T.; Noh, S. H.; Tanabe, T.; Han, B.; Nien, C. Y.; Ohsaka, T.; Matsumoto, F. Enhanced Electrocatalytic Activity of Carbon-Supported Ordered Intermetallic Palladium−Lead (Pd_3Pb) Nanoparticles toward Electrooxidation of Formic Acid. *Chem. Mater.* **2017**, *29*, 2906−2913.

(9) Kang, Y.; Pyo, J. B.; Ye, X.; Gordon, T. R.; Murray, C. B. Synthesis, Shape control, and Methanol Electro-oxidation Properties of Pt-Zn Alloy and Pt_3Zn Intermetallic Nanocrystals. *ACS Nano* **2012**, *6*, 5642−7.

(10) Kim, D.; Xie, C.; Becknell, N.; Yu, Y.; Karamad, M.; Chan, K.; Crumlin, E. J.; Nørskov, J. K.; Yang, P. Electrochemical Activation of CO_2 through Atomic Ordering Transformations of AuCu Nanoparticles. *J. Am. Chem. Soc.* **2017**, *139*, 8329−8336.

(11) Furukawa, S.; Komatsu, T. Intermetallic Compounds: Promising Inorganic Materials for Well-Structured and Electronically

DOI: 10.1021/jacs.8b09919
J. Am. Chem. Soc. 2019, 141, 2342−2347

Modified Reaction Environments for Efficient Catalysis. *ACS Catal.* **2017**, *7*, 735−765.
(12) Tsai, A. P.; Kameoka, S.; Nozawa, K.; Shimoda, M.; Ishii, Y. Intermetallic: A Pseudoelement for Catalysis. *Acc. Chem. Res.* **2017**, *50*, 2879−2885.
(13) Cui, Z.; Li, L.; Manthiram, A.; Goodenough, J. B. Enhanced Cycling Stability of Hybrid Li-air Batteries Enabled by Ordered Pd_3Fe Intermetallic Electrocatalyst. *J. Am. Chem. Soc.* **2015**, *137* (23), 7278−81.
(14) Chen, H.; Wang, D.; Yu, Y.; Newton, K. A.; Muller, D. A.; Abruna, H.; DiSalvo, F. J. A Surfactant-Free Strategy For Synthesizing and Processing Intermetallic Platinum-Based Nanoparticle Catalysts. *J. Am. Chem. Soc.* **2012**, *134* (44), 18453−9.
(15) Ji, X.; Lee, K. T.; Holden, R.; Zhang, L.; Zhang, J.; Botton, G. A.; Couillard, M.; Nazar, L. F. Nanocrystalline Intermetallics on Mesoporous Carbon for Direct Formic Acid Fuel Cell Anodes. *Nat. Chem.* **2010**, *2*, 286.
(16) Maligal-Ganesh, R. V.; Xiao, C.; Goh, T. W.; Wang, L.-L.; Gustafson, J.; Pei, Y.; Qi, Z.; Johnson, D. D.; Zhang, S.; Tao, F.; Huang, W. A Ship-in-a-Bottle Strategy To Synthesize Encapsulated Intermetallic Nanoparticle Catalysts: Exemplified for Furfural Hydrogenation. *ACS Catal.* **2016**, *6*, 1754−1763.
(17) Wang, C.; Chen, D. P.; Sang, X.; Unocic, R. R.; Skrabalak, S. E. Size-Dependent Disorder−Order Transformation in the Synthesis of Monodisperse Intermetallic PdCu Nanocatalysts. *ACS Nano* **2016**, *10*, 6345−6353.
(18) Mosby, J. M.; Prieto, A. L. Direct Electrodeposition of Cu_2Sb for Lithium-Ion Battery Anodes. *J. Am. Chem. Soc.* **2008**, *130*, 10656−10661.
(19) Tolegen, B.; Adi, A.; Aishova, A.; Bakenov, Z.; Nurpeissova, A. Electrodeposited Ni-Sn Intermetallic Alloy Electrode for 3D Sulfur Battery. *Mater. Today* **2017**, *4*, 4491−4495.
(20) Li, G.-R.; Zheng, F.-L.; Tong, Y.-X. Controllable Synthesis of Bi_2Te_3 Intermetallic Compounds with Hierarchical Nanostructures via Electrochemical Deposition Route. *Cryst. Growth Des.* **2008**, *8*, 1226−1232.
(21) Hwang, S.-M.; Bonevich, J. E.; Kim, J. J.; Moffat, T. P. Electrodeposition of $Pt_{100-x}Pb_x$ Metastable Alloys and Intermetallics. *J. Electrochem. Soc.* **2011**, *158*, D307−D316.
(22) Golodnitsky, D.; Gudin, N. V.; Volyanuk, G. A. Study of Nickel-Cobalt Alloy Electrodeposition from a Sulfamate Electrolyte with Different Anion Additives. *J. Electrochem. Soc.* **2000**, *147*, 4156−4163.
(23) Bredael, E.; Blanpain, B.; Celis, J. P.; Roos, J. R. On the Amorphous and Crystalline State of Electrodeposited Nickel-Phosphorus Coatings. *J. Electrochem. Soc.* **1994**, *141*, 294−299.
(24) Tian, N.; Zhou, Z.-Y.; Yu, N.-F.; Wang, L.-Y.; Sun, S.-G. Direct Electrodeposition of Tetrahexahedral Pd Nanocrystals with High-Index Facets and High Catalytic Activity for Ethanol Electrooxidation. *J. Am. Chem. Soc.* **2010**, *132*, 7580−7581.
(25) Landolt, D. Electrodeposition Science and Technology in the Last Quarter of the Twentieth Century. *J. Electrochem. Soc.* **2002**, *149*, S9−S20.
(26) Sander, M. S.; Prieto, A. L.; Gronsky, R.; Sands, T.; Stacy, A. M. Fabrication of High-Density, High Aspect Ratio, Large-Area Bismuth Telluride Nanowire Arrays by Electrodeposition into Porous Anodic Alumina Templates. *Adv. Mater.* **2002**, *14*, 665−667.
(27) Yan, Y.; Du, J. S.; Gilroy, K. D.; Yang, D.; Xia, Y.; Zhang, H. Intermetallic Nanocrystals: Syntheses and Catalytic Applications. *Adv. Mater.* **2017**, *29*, 1605997.
(28) Wang, D.; Xin, H. L.; Hovden, R.; Wang, H.; Yu, Y.; Muller, D. A.; DiSalvo, F. J.; Abruña, H. D. Structurally Ordered Intermetallic Platinum−Cobalt Core−Shell Nanoparticles with Enhanced Activity and Stability as Oxygen Reduction Electrocatalysts. *Nat. Mater.* **2013**, *12*, 81.
(29) Cui, Z.; Chen, H.; Zhao, M.; DiSalvo, F. J. High-Performance Pd_3Pb Intermetallic Catalyst for Electrochemical Oxygen Reduction. *Nano Lett.* **2016**, *16*, 2560−2566.
(30) Bu, L.; Zhang, N.; Guo, S.; Zhang, X.; Li, J.; Yao, J.; Wu, T.; Lu, G.; Ma, J.-Y.; Su, D.; Huang, X. Biaxially Strained PtPb/Pt Core/Shell Nanoplate Boosts Oxygen Reduction Catalysis. *Science* **2016**, *354* (6318), 1410−1414.
(31) Kragten, J. The Stability Constant of Pd-EDTA. *Talanta* **1978**, *25*, 239−240.
(32) Mech, K.; Żabiński, P.; Kowalik, R.; Fitzner, K. Kinetics and Mechanism of $[PdCl_x(H_2O)_{4-x}]_{2-x}$ (x = 3,4) Complexes Electro-Reduction. *J. Electrochem. Soc.* **2013**, *160*, H770−H774.
(33) Heise, M.; Chang, J.-H.; Schönemann, R.; Herrmannsdörfer, T.; Wosnitza, J.; Ruck, M. Full Access to Nanoscale Bismuth−Palladium Intermetallics by Low-Temperature Syntheses. *Chem. Mater.* **2014**, *26*, 5640−5646.
(34) Schubert, K. *Kristallstrukturen Zweikomponentiger Phasen*; Springer: 1964.
(35) Sarah, N.; Schubert, K. Kristallstruktur von Pd_5Bi_2. *J. Less-Common Met.* **1979**, *63*, P75−P82.
(36) Okamoto, H. The Bi-Pd (Bismuth-Palladium) System. *J. Phase Equilib.* **1994**, *15*, 191−194.
(37) Landolt, D. Electrodeposition Science and Technology in the Last Quarter of the Twentieth Century. *J. Electrochem. Soc.* **2002**, *149*, S9.
(38) Ge, X.; Sumboja, A.; Wuu, D.; An, T.; Li, B.; Goh, F. W. T.; Hor, T. S. A.; Zong, Y.; Liu, Z. Oxygen Reduction in Alkaline Media: From Mechanisms to Recent Advances of Catalysts. *ACS Catal.* **2015**, *5*, 4643−4667.
(39) Fletcher, S. Tafel Slopes from First Principles. *J. Solid State Electrochem.* **2009**, *13*, 537−549.
(40) Gileadi, E. *Physical Electrochemistry: Fundamentals, Techniques and Applications*; Wiley-VCH: Weinheim, 2011; pp 78−79.
(41) Holewinski, A.; Linic, S. Elementary Mechanisms in Electrocatalysis: Revisiting the ORR Tafel Slope. *J. Electrochem. Soc.* **2012**, *159*, H864−H870.
(42) Wei, G.-F.; Fang, Y.-H.; Liu, Z.-P. First Principles Tafel Kinetics for Resolving Key Parameters in Optimizing Oxygen Electrocatalytic Reduction Catalyst. *J. Phys. Chem. C* **2012**, *116*, 12696−12705.
(43) Jaksic, J. M.; Ristic, N. M.; Krstajic, N. V.; Jaksic, M. M. Electrocatalysis for Hydrogen Electrode Reactions in the Light of Fermi Dynamics and Structural Bonding FACTORS—I. Individual Electrocatalytic Properties of Transition Metals. *Int. J. Hydrogen Energy* **1998**, *23*, 1121−1156.

DOI: 10.1021/jacs.8b09919
J. Am. Chem. Soc. 2019, 141, 2342−2347